Holographic display with tilted spatial light modulator

1 author:

Tomasz Kozacki
Warsaw University of Technology
128 PUBLICATIONS   **992** CITATIONS

SEE PROFILE

Some of the authors of this publication are also working on these related projects:

Master Thesis View project

Holographic display with tilted spatial light modulator

Tomasz Kozacki

Institute of Micromechanics and Photonics, Warsaw University of Technology, 8 Świętego Andrzeja Boboli Street,
02-525 Warsaw, Poland (t.kozacki@mchtr.pw.edu.pl)

In this paper, we analyze a holographic display system utilizing a phase-only spatial light modulator (SLM) based on liquid crystal on silicon (LCoS). An LCoS SLM works in reflection, and, in some applications, it is convenient to use with an inclined illumination. Even with a highly inclined illumination, the holographic display is capable of good-quality image generation. We show that the key to obtain high-quality reconstructions is the tilt-dependent calibration and algorithms. Typically, an LCoS SLM is illuminated with a plane wave with normal wave vector. We use inclined illumination, which requires development of new algorithms and display characterization. In this paper we introduce two algorithms. The first one is designed to process a digital hologram captured in CCD normal configuration, so it can be displayed in SLM tilted geometry, while the second one is capable of synthetic hologram generation for tilted SLM configuration. The inclined geometry asymmetrically changes the field of view of a holographic display. The presented theoretical analysis of the aliasing effect provides a formula for the field of view as a function of SLM tilt. The incidence angle affects SLM performance. Both elements of SLM calibration, i.e., pixel phase response and wavefront aberrations, strongly depend on SLM tilt angle. The effect is discussed in this paper. All of the discussions are accompanied with experimental results.   © 2011 Optical Society of America

OCIS codes: 090.2870, 110.3010.

1. Introduction

People wish to be entertained in the three-dimensional world. They want to see three-dimensional (3D) images in televisions as observed in the real world. One of the promising future technologies is holographic displays [1,2]. The holographic technique works with complex optical waves such as those generated in the real world and therefore correctly reconstructs 3D object wavefronts. In holographic displays wavefronts representing an object are reproduced with spatial light modulators (SLMs). SLMs based on liquid crystal on silicon (LCoS) have been recognized as the most feasible devices for holographic displays [3]. These devices work in reflection and are capable of phase modulation of an illuminating wave in the range of $0–2\pi$ (and even more). This allows us to address them directly with the phase of an object wavefront. However, due to limited resolution and aperture, angular view ability of a single

SLM holographic display is the main problem affecting the experience of observing optically reconstructed holographic images. To overcome this, several attempts have been made to enhance this feature by employing innovative optical holographic display modules with several tilted SLMs [4–6]. LCoS SLMs work in reflection, and it is often convenient to use them with inclined illumination. This can make optical system designs easier as well as minimize the quantity of necessary optical elements in an optical path. In order to make use of holographic displays, employing LCoS SLMs tilted against an illuminating beam, three main issues have to be considered:

–   The necessity of the LCoS SLM calibration depending on the tilt value, this includes calibration of pixel response and wavefront aberration.
–   Characterization of tilt-dependent imaging space.
–   Modification of an object wavefront calculated from captured digital holograms in order to allow their reconstruction at the tilted SLM display; this

topic is extended to the algorithm of computer-generated holograms (CGHs) for inclined SLM geometry.

In the paper we address all these issues. In Sections 3 and 4 we provide equations for both algorithms: for digital hologram processing and for CGHs. Section 5 is devoted to calibration issues of an SLM for inclined illumination. Additionally in Section 6, we study the field of view (FoV) of a holographic display system utilizing a tilted LCoS SLM to define its imaging space. We have found that the FoV is tilt dependent and asymmetrical. All theoretical predictions and algorithms are tested experimentally. We present experimental results proving that, even with highly off-axis illumination, the holographic display with a tilted SLM can generate images of good quality. We believe that this discussion is interesting and new in the literature.

2. Holographic Display in Tilted SLM Geometry

In this paper we study an SLM-based holographic display schematically presented in Fig. 1. In the system the reflective phase-only LCoS SLM (model HEO 1080P) is illuminated by a linearly polarized inclined plane wave (wave vector oriented in plane $x'\mathbf{N}$). The SLM has high-definition resolution (1920× 1080) with pixel pitch $\Delta = 8\,\mu\mathrm{m}$. Its molecules change their axis orientation in the plane $y'\mathbf{N}$. We apply two linear polarization maintaining devices: the input half-wave plate and the output polarizer. In the display SLM, pixels are addressed with the phase of the object wave. We use the assumption that phase distribution at a plane distant from the object carries the majority of the information. This representation is quite accurate for scattering objects [7] and allows us to produce images of good quality. In our system, however, we introduce highly off-axis SLM tilt, which influences performance of LCoS displays [8] and decreases the quality of holographic imaging.

We address SLM pixels with object wave phase values, which may be delivered by means of a digital holographic acquisition system as well as by numerical generation of synthetic holograms. Let
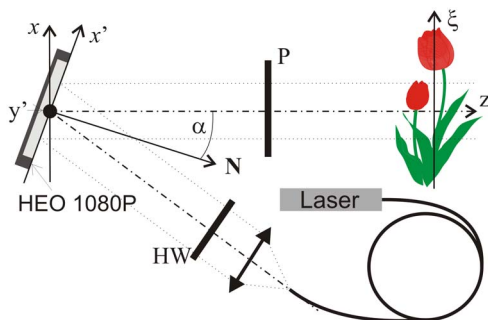

Fig. 1. (Color online) Experimental setup for holographic image generation with tilted SLM; laser, 532 nm; HW, half-wave plate; P, polarizer; $X'(x', y')$ is a plane of an SLM and $\Xi(\xi, n)$ of the reconstruction.

us now consider the imaging of the real object wave, captured with digital holography, where we acquire intensity fringes. In order to optimally reconstruct a captured digital hologram with a phase-only modulator, we filter a complex object beam from a captured hologram using numerical techniques [9] or phase-shifting digital holography [10]. Then, in the reconstruction step, we use the phase of an object beam only.

3. Processing of Digital Hologram to Tilted Display Geometry

The optical axis of the display system is located at an angle θ to the SLM's normal (Fig. 1). The angle θ violates the Fresnel approximation. As a result, the reflected and refracted light from the SLM generates an off-axis field, which is paraxial around the optical axis. In the digital inline holography, the CCD captures an object wave scattered in normal direction to the detector. For off-axis holography, the off-axis angle is small. Therefore, in order to display the digital hologram in a tilted configuration, first we have to process it numerically to the tilted geometry of the SLM.

In our display, the optical object wave is reproduced with the tilted SLM and the highly off-axis plane-wave illumination. This results in a nonparaxial field at SLM plane X', which is paraxial around the optical axis z. Using digital holography, we capture the optical field at plane X; for reconstruction we need to propagate it to tilted plane X'.

In this section we first give the general formula for field propagation between planes X and X' and back, where a field paraxiality is employed. We assume that the optical field at plane X' is paraxial along the plane-wave carrier:

$$u(\mathbf{x}') = u_p(\mathbf{x}') \exp(2\pi i \mathbf{x}' \cdot \mathbf{f}_c), \qquad (1)$$

where $u_p(\mathbf{x}')$ denotes optical field components of low frequency. Application of the nonparaxial propagation algorithm leads to a very high sampling rate.

Let us consider diffraction in a linear, homogeneous, and isotropic medium where a plane-wave spectrum (PWS) [11] is related to optical field $u(\mathbf{x}')$ by equation

$$U^X(\mathbf{f}') = \int_{-\infty}^{\infty} \int u(\mathbf{x}') \exp\{-i 2\pi \mathbf{f} \cdot \mathbf{x}'\} \mathrm{d}\mathbf{x}', \qquad (2)$$

where corresponding vectors are given by $\mathbf{x}' = x\hat{e}_x + y\hat{e}_y$, $\mathbf{f}' = f'_x \hat{e}_x + f'_y \hat{e}_y$, $\hat{e}$ is the unit vector, and the dot denotes the vector scalar product. The spatial frequencies $\mathbf{f}$ are connected with the wave vector via $\mathbf{k}_i = 2\pi(\hat{e}_x f'_x + \hat{e}_y f_{y'} + \hat{e}_z(\lambda^{-2} - \mathbf{f}' \cdot \mathbf{f}')^{1/2})$. Within this paper the evanescent waves are disregarded.

The algorithm of field propagation between tilted planes [12] consists of simple remapping of PWS components of optical fields at SLM plane $U^{X'}(\mathbf{f}')$ and the plane normal to optical axis $U^X(\mathbf{f})$, using rotational coordinate transformation. The nonlinearity of

rotational transformation requires the application of Jacobian; however, it can be neglected if the processed field is paraxial [13].

If $\mathbf{T}^-$ is a matrix used to transform transverse frequency coordinates of optical field at the plane X into frequency coordinates of tilted plane X', then the frequency of both vectors can be remapped with

$$\mathbf{f}' = \mathbf{T}^-[\mathbf{f}] + \mathbf{f}_c, \qquad (3)$$

where

$$\mathbf{T}^{\pm} = \begin{bmatrix} a_1^{\pm} & a_2^{\pm} & a_3^{\pm} \\ a_4^{\pm} & a_5^{\pm} & a_6^{\pm} \\ a_7^{\pm} & a_8^{\pm} & a_9^{\pm} \end{bmatrix}.$$

The superscript $+$ assigns matrix coefficients of forward propagation: X' to X. The rotation matrix around y axis is simply

$$\mathbf{T}^{\pm} = \begin{bmatrix} \cos\theta & 0 & \pm\sin\theta \\ 0 & 1 & 0 \\ \pm\sin\theta & 0 & \cos\theta \end{bmatrix}. \qquad (4)$$

For rotation around the y axis, the PWS carrier is $\mathbf{f}_c = [f_{cx} = \sin(\theta)\lambda^{-1}, f_{cy} = 0]$. For two-axis rotation, the coefficients are given in [14]. Using this nonlinear remapping, we can associate PWS components of optical fields at both mutually tilted planes:

$$f_{x}' = \alpha^-(f_x, f_y) + f_{cx}$$
$$= a_1^- f_x + a_2^- f_y + a_3^-(\lambda^{-2} - f_x^2 - f_y^2)^{1/2} + f_{cx},$$
$$f_{y}' = \beta^-(f_x, f_y) + f_{cx}$$
$$= a_4^- f_x + a_5^- f_y + a_6^-(\lambda^{-2} - f_x^2 - f_y^2)^{1/2} + f_{cy}. \qquad (5)$$

With this formula we relate PWS components of the low-frequency field at SLM plane $U_p^{X'}(\mathbf{f}')$ to the ones at beam normal. The low-frequency field at the plane X' is the one to be loaded to the SLM. Finally, we write a compact formula for optical field propagation (transfer of plane-wave spectra) between tilted planes X and X',

$$U_p^{X'}(f_x', f_y') = U^X(\alpha^-(f_x, f_y) + f_{cx}, \beta^-(f_x, f_y) + f_{cy}), \quad (6)$$

and between X' and X,

$$U^X(f_x, f_y) = U_p^{X'}(\alpha^+(f_x' - f_{cx}, f_y' - f_{cy}), \beta^+(f_x' - f_{cx}, f_y' - f_{cy})). \qquad (7)$$

Application of Eqs. (6) and (7) results in nonlinearly distributed nodes of the PWS. These nodes have to be mapped into a uniformly spaced frequency grid using interpolation methods [15] before application of the inverse Fourier transform. The algorithm for processing an object wave captured with digital holography is constructed with direct application of Eq. (6), frequency nodes interpolation, and compu-

tation of the discrete Fourier transform. To reconstruct the digital hologram, we load a tilted SLM with phase values of field given by the discrete Fourier transform.

The detector (CCD) and the SLM provide different sampling of the optical field. The wavelengths in both acquisition and display processes can be different as well. However, both device's space bandwidth products are comparable. Thus, to reduce interpolation error and maximize reconstruction signal space bandwidth product, we use captured holographic signal as if it was acquired with SLM sampling. This simply causes the reconstructed image to be transversely and laterally magnified [16].

4. Algorithm for CGH for Tilted SLM Configuration

We now apply results derived in Section 3 to design an algorithm for CGH for tilted plane geometry. We apply the well-known CGH Gerchberg–Saxton algorithm [17], in which known intensity distributions at object and SLM planes are iteratively applied. Within the algorithm, an optical field u is propagated between planes X' and Ξ (Fig. 1). At planes X' and Ξ, the amplitude distributions are imposed. We assume that SLM is phase-only; this is represented with the amplitude rectangular aperture function $A_0(x', y')$. At the reconstruction plane, we wish to obtain the image of intensity distribution $B_0(\xi, \eta)$.

Applying the results of Section 3 [Eqs. (6) and (7)], we provide formulas for the nth iteration of the CGH algorithm. Algorithm steps are illustrated in Fig. 2.

At step 1 of the algorithm, we apply SLM amplitude constrains $A_0(x', y')$ and compute the PWS,

$$U_p^{X'(n)}(f_x', f_y') = \iint A_0(x', y') \exp\{i\mathrm{ARG}(\bar{u}_p^{(n-1)}(x', y'))\}$$
$$\times \exp\{-2\pi i(f_x'x' + f_y'y')\}\mathrm{d}x'\mathrm{d}y', \qquad (8)$$

of low-frequency paraxial field $\bar{u}_p^{(n-1)}(x', y')$ around plane-wave carrier $[f_{cx}, f_{cy}]$. The plane-wave carrier is defined in Eq. (3).

In step 2 [Eqs. (9) and (10)], we propagate the resulting PWS from plane X' to the image plane Ξ. The propagation is obtained in two numerical
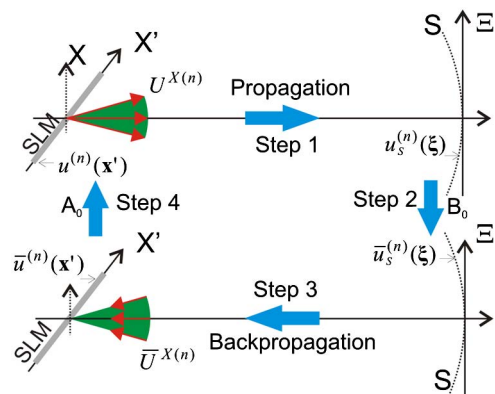

Fig. 2. (Color online) Illustration of algorithm steps for generation of CGH for tilted SLM.

procedures: propagation between tilted planes,

$$U^{X(n)}(f_x, f_y) = U_p^{X'(n)}(\alpha^+(f_x' - f_{cx}, f_y' - f_{cy}),$$
$$\beta^+(f_x' - f_{cx}, f_y' - f_{cy})), \qquad (9)$$

and the Fresnel propagation,

$$u_S^{(n)}(\xi, \eta) = (\lambda z)^{-1} \iint \iint U^{X(n)}(f_x, f_y)$$
$$\times \exp\{2\pi i(f_x x + f_y y)\} \mathrm{d}f_x \mathrm{d}f_y$$
$$\times \exp\left\{\frac{ik}{2z}(x^2 + y^2)\right\}$$
$$\times \exp\left\{-\frac{ik}{z}(x\xi + y\eta)\right\} \mathrm{d}x \mathrm{d}y, \qquad (10)$$

where $u_S^{(n)}(x, y)$ denotes an optical field at spherical surface S in the image plane. Frequency nodes, results of Eq. (9), are nonlinearly distributed; they have to be mapped to a uniformly sampled grid using interpolation methods before assembling them into the optical field at the plane X and computation of propagation by distance z using the Fresnel approximation [Eq. (10)]. The Fresnel propagation is performed with a direct method [18]. We compute the major part of the Fresnel propagation only. The field is propagated to the spherical surface S [19]; we do not multiply it by chirp function at the plane Ξ. This is unnecessary since, in the backward propagation, there is conjugate chirp nulling the effect of the first one. In the Fresnel region, amplitude constrains can be applied at surface S as well as at plane Ξ. Moreover, our algorithm is designed for an image distance $z > N\Delta^2\lambda^{-1}$, where Fresnel propagation chirp sampling is violated [20]. The condition is fulfilled by most of the holographic systems. For shorter distances, the SLM gives aliasing images, and the display spatial bandwidth is not fully used [21].

In the third step, the image amplitude constrains (B_0), basing on error-reduction algorithms, are applied:

$$\bar{u}_S^{(n)}(\xi, \eta) = B_0(\xi, \eta) \exp\{i\mathrm{ARG}(u_S^{(n)}(\xi, \eta))\}. \qquad (11)$$

The techniques with better convergence [22] are not giving an experimental image improvement. The level of SLM phase reproduction error is too high. In step 4, we backpropagate the optical field from surface S to the SLM plane (X'), using the same technique as in step 2 [Eqs. (9) and (10)]. First, we propagate the field from surface S to parallel plane X, and then we compute the PWS:

$$\bar{U}^{X(n)}(f_x, f_y) = \lambda z \iint \iint \bar{u}_S^{(n)}(\xi, \eta)$$
$$\times \exp\left\{\frac{ik}{z}(x\xi + y\eta)\right\} \mathrm{d}\xi \mathrm{d}\eta$$
$$\times \exp\left\{\frac{-ik}{2z}(x^2 + y^2)\right\}$$
$$\times \exp\{-2\pi i(f_x x + f_y y)\} \mathrm{d}x \mathrm{d}y. \qquad (12)$$

The obtained PWS is propagated to the tilted SLM plane X',

$$\bar{U}_p^{X'(n)}(f_x', f_y') = \bar{U}^{X(n)}(\alpha^-(f_x, f_y) + f_{cx}, \beta^-(f_x, f_y) + f_{cy}), \qquad (13)$$

and then assembled to the paraxial field (around plane-wave carrier $[f_{cx}, f_{cy}]$) using the discrete Fourier transform

$$\bar{u}_p^{(n)}(x', y') = \iint \bar{U}_p^{X'(n)}(f_x', f_y') \exp\{2\pi i(f_x' x' + f_y' y')\} \mathrm{d}f_x' \mathrm{d}f_y'. \qquad (14)$$

This field is then processed in step 1 of the algorithm. Usually 10–20 iterations are sufficient to give satisfactory image quality.

5. SLM Calibration for Tilted Configuration

A proper SLM calibration is necessary for high-quality imaging of an LCoS SLM-based holographic display. The procedure includes calibration of SLM curvature (wavefront aberration) and calibration of nonlinearity of the SLM phase response. Both factors depend on the SLM tilt angle. There are many approaches that can be applied for these tasks. For the calibration of wave aberration we apply a Twyman–Green-based interferometric method [23], while for characterization of the nonlinearity of phase response, we use a double slit experiment [24].

A. Calibration of Wavefront Aberration

The measurement of wavefront aberration can be problematic when a large tilt of the SLM is introduced. Using a 5 cm beam splitter cube, we were able to measure SLM curvature for 10° tilt only. Moreover, characterization for every angle is time consuming. Therefore, we propose to characterize SLM curvature for normal orientation only and then recalculate it to an inclined plane.

The procedure starts with the experimental characterization of wavefront aberration of an SLM with normal illumination. The exemplary captured SLM wavefront is presented in Fig. 3. The aberration gives instantly the height function of the SLM employing thin element approximation (TEA). The height function of the SLM can be used to calculate wave aberration obtained with inclined illumination as well. This can be done numerically by applying the Born scattering approximation method [25]. In the
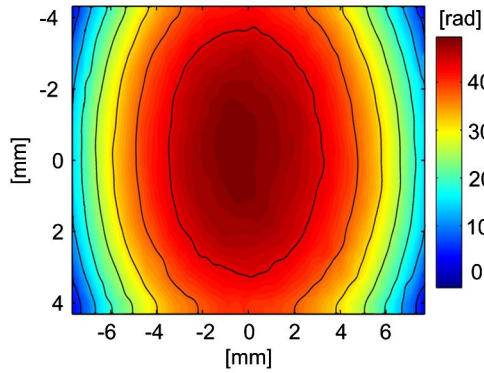
Fig. 3. (Color online) Measured wavefront aberration for normal SLM orientation in radians; contour step corresponds to 2π phase increment.

method, locally refracted plane-wave components are computed and then assembled into the output field. The case of reflection from the tilted SLM is visualized in Ewald's sphere in Fig. 4. The application of such an approach can be problematic. We have to implement the propagation method, whose computation time is long. Therefore, we propose to use the TEA for a tilted SLM. The method can be derived using Born approximation with an assumption that all reflected wave vectors have the same direction $(-\theta)$. Then, due to SLM curvature, only the phase of the illuminating plane wave is altered. This gives us the distribution of tilt-dependent SLM wave aberration at plane X',

$$u(x',y') = \exp\{ik2h(x',y')\cos(\theta)\}, \qquad (15)$$

where $h(x',y')$ is an SLM height function obtained from an interferometric experiment with normal illumination. To remove the aberration effect, we write the conjugate phase of the result. This nulls the influence of tilt-dependent wave aberration.

In Fig. 5 we present an effect of wavefront aberration compensation; there are focal images received for a spherical wave (focal 462 mm) applied to the tilted SLM ($\theta = 20°$). The image in Fig. 5(a) is obtained with the application of the proposed aberration
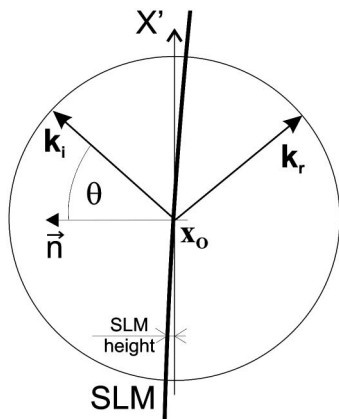

Fig. 4. Ewald sphere for plane-wave reflection from tilted SLM; $\mathbf{k_i}$ and $\mathbf{k_r}$, illumination and reflection local wave vectors.
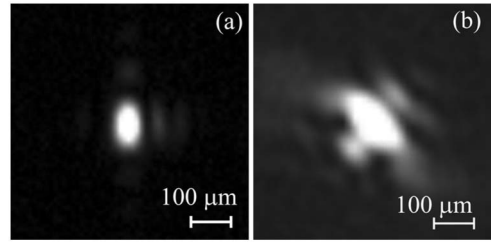

Fig. 5. Comparison of focal point images for spherical wave (focal 462 mm) produced by SLM tilted by 20° with applied wavefront aberration compensation (a) with tilt correction, (b) without tilt correction.

compensation based on Eq. (15). For comparison, in Fig. 5(b) we show the focal image received with applied wavefront aberration compensation without proposed tilt correction.

Let us now test the accuracy of the proposed TEA for measured curvature and SLM tilt of 30° by application of the Born scattering approximation method. We have computed the difference between wave aberration obtained using the proposed tilted TEA method and the one using the Born scattering approximation. We have computed the phase difference, and we have obtained a peak-to-valley ratio of 0.01 rad. This is a small deviation, which shows that application of a tilted TEA is sufficient. Tilt of 30° is a very large angle for a physical SLM due to large cross talk between neighboring pixels. The 1080P SLM is composed of a liquid crystal layer of depth $2\,\mu m$. This pixel depth results in tilt-dependent pixel cross talk. We define pixel cross talk as the percentage of light that enters one pixel and goes out in the another one to entire pixel light illumination. For the tilt angle of 30°, pixel cross talk exceeds 50%.

B. SLM Response Calibration

The 1080P SLM is based on nematic liquid crystal, and it is designed for normal illumination. It gives a phase modulation for inclined illumination as well. In this case, it is necessary to calibrate the SLM for every tilt angle. We have characterized calibration curves for different SLM tilts, i.e., $\theta = 0°$, 10°, 20°, 30°, 45°; the combined results are presented in Fig. 6. All measurements were performed for the same voltage range, 0 V to 2.59 V. The value of 2.59 V is a minimal voltage for which 2π modulation is obtained for 45° tilt of the SLM. For comparison, a normally oriented SLM generates phase modulation of 3.05π rad in this voltage range.

Let us now consider use of 0° calibration curve for a tilted SLM. For the voltage in the range 1.34 V to 2.37 V, a normally oriented SLM provides the phase difference of 2π. If we use this voltage range for a 10° tilted SLM, the phase difference is reduced to 1.97π; i.e., we introduce phase error equal to $\lambda/67$. Error of this magnitude is negligible. However, for 20° SLM tilt and the same range of voltages, we can get maximum phase modulation of 1.86π. This corresponds to
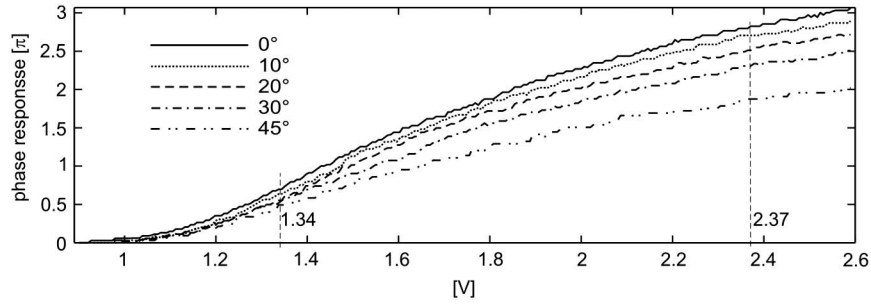
Fig. 6. Pixel phase response calibration for series of angular orientation of SLM, $\theta = 0°$, $10°$, $20°$, $30°$, $45°$ and voltage range of 0–2.59 V.

the phase maximum error of $\lambda/14$, which is unacceptable.

In Fig. 7 we present reconstructions of CGHs in a tilted SLM holographic display ($\theta = 20°$). The hologram was designed with the algorithm outlined in Section 4. To receive the image in Fig. 7(a), we have applied the phase calibration curve for $20°$ tilt. For comparison, in Fig. 7(b) we show a reconstructed image obtained with applied phase calibration curve for $0°$. It can be noticed that improper calibration curve effects increase noise and zero order.

6. FoV

In case of a tilted SLM display, the cone of a PWS generated with an SLM is asymmetric. This suggests that an imaging parameter such as FoV is asymmetric and angle dependent. There are two definitions of the FoV that can characterize a holographic display: FoV and extended FoV (EFoV). For FoV we have adopted the "standard" definition of maximum object size that can be recorded with digital holography [26]. The standard FoV is defined by an imaging size where an aliasing image is not generated. In this case a hologram can be thought of as an assembly of well-sampled spherical waves. It means that all of the point images within the FoV will have the same intensity and resolution. Therefore, images located within the FoV will not have quality losses. Within the EFoV, the aliasing images appear. The alias images are however localized outside of the EFoV (outside of the image), and they are not disturbing the viewing of a holographic reconstruction. Additionally, they are of lower intensity and

resolution than original images. Some of the SLM bandwidth is used to generate aliasing images. Therefore, images located within an area outside of the FoV and inside the EFoV have smaller intensity and resolution than the ones located inside of the FoV. The analysis of the effect for normal SLM illumination is presented elsewhere [21]. For presentation simplicity, the analysis of the FoV is one dimensional, and the rotation is around the y axis. For the x axis, the number of pixels is $N = 1920$. The analysis can be extended to two dimensions.

A. Standard FoV

In this imaging area, all of the SLM pixels participate in the generation of point images within the FoV; there is no loss in resolution. These point images are formed by well-sampled spherical wavefronts. Therefore, at the SLM border, the local spatial frequency of a spherical wave generating point images at the FoV limits ($\xi_{\text{FOV}}^{\pm}$) have to meet the following criterion:

$$f_l(x') = \frac{\partial \phi(x')}{2\pi \partial x'} = \frac{\partial R(x', \xi_{\text{FOV}}^{\pm})}{\lambda \partial x'}$$
$$= \begin{cases} \lambda^{-1} \sin \theta + (2\Delta)^{-1} & \text{for} \quad x' = x'^+, \\ \lambda^{-1} \sin \theta - (2\Delta)^{-1} & \text{for} \quad x' = x'^-. \end{cases} \quad (16)$$

R is a geometrical distance between the SLM pixel and image point; $x'^{\pm}$ are coordinates of left and right SLM pixels ($N\Delta = x'^+ - x'^-$). By performing some arithmetical manipulations, we get the formula for left $\varepsilon_{\text{FOV}}^-$ and right $\varepsilon_{\text{FOV}}^+$ FoV bounds:
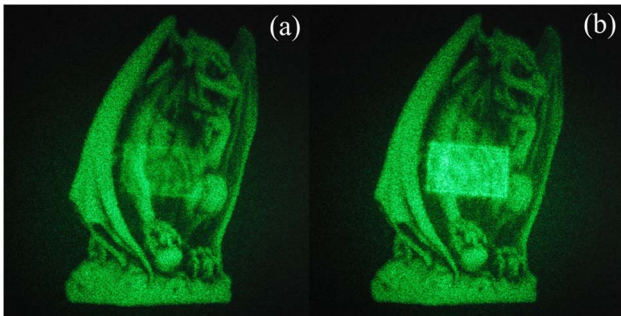

Fig. 7. (Color online) Comparison of image reconstruction of CGH reconstructed in holographic display with tilted SLM ($\theta = 20°$) with (a) applied proper calibration curve for $20°$ and (b) for $0°$.
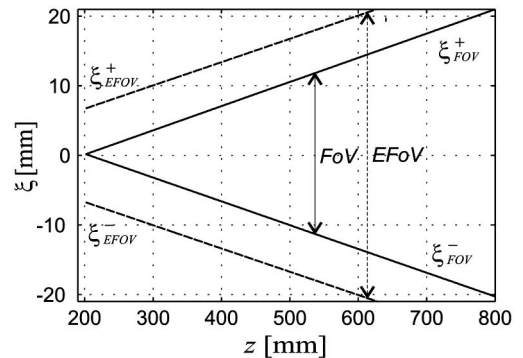

Fig. 8. Plot of the FoV and the EFoV for $\theta = 25°$ as a function of reconstruction distance.

$$\xi_{\text{FOV}}^{\pm} = \frac{x'^{\mp} - z\sin\theta - z\cos\theta\tan\beta^{\pm}}{\cos\theta - \sin\theta\tan\beta^{\pm}}, \qquad (17)$$

where $\beta^{\pm} = \sin^{-1}(-\sin\theta \mp \lambda(2\Delta)^{-1})$ denote angles corresponding to maximum local spatial frequency. The FoV is simply $\xi_{\text{FOV}}^{+} - \xi_{\text{FOV}}^{-}$. Limits of the FoV from the left and right sides are different. The FoV bounds are plotted as a function of reconstruction distance with a solid line in Fig. 8 for $\theta = 25°$. Limit ξ_{FOV}^{+} is further from the optical axis. Let us analyze the FoV for an exemplary situation for reconstruction distance of 500 mm. For the series of angles $\theta = 0°$, $15°$, $30°$, and $45°$, the values of the FoV are 15.9, 17.5, 22.8, and 33.4 mm, respectively. In Fig. 8 there are bounds of EFoV (dashed line), discussed in Subsection 6.B as well.

By using Eq. (17) and setting $\xi_{\text{FOV}}^{+} - \xi_{\text{FOV}}^{-} = 0$, we can estimate the minimum imaging distance $z_{\min}$ where the FoV is zero:

$$z_{\min} = B_x \frac{\cos\theta - 0.5\sin\theta(\tan\beta^{+} + \tan\beta^{-})}{\tan\beta^{-} - \tan\beta^{+}}. \qquad (18)$$

The distance of minimum reconstruction becomes shorter as the tilt angle increases. It can also be shown that the center of the FoV is above the optical axis (for distance $z_{\min}$ the FoV is a point image above the optical axis). For the series of angles $\theta = 0$, $15°$, $30°$, and $45°$, corresponding distances $z_{\min}$ are 246, 229, 184, and 122 mm, respectively.

B. EFoV

The images within the FoV are free of aliasing sources; however, the size of the imaging area is small, especially for short reconstruction distances. We therefore consider the imaging area outside of the FoV. The image formed in this area always generates a related aliasing image. We can use some of this area for FoV extension. The idea is that aliased images shall be generated outside of the EFoV. The aliased images are related to the image within the EFoV part only. Moreover, the aliased images have lower intensity and resolution than original ones.

For FoV extension criteria, the image part at the border of the EFoV shall generate aliased images at the border as well. This is however not entirely possible for the display in a tilted configuration. The aliased image distance varies with the position of the point image. The values are meaningfully different for left and right FoV extensions. Moreover, the aliasing images are focused in different (longitudinally displaced) planes than the object one.

To find boundaries of the FoV extension, we have to find distances of aliased point images first. This can be computed by the application of the local spatial frequency of a spherical wave generated with the SLM. We consider an image point at position ξ_0 resulting from the spherical wavefront. This wavefront has simply a local ray parallel to the optical axis at $x' = \xi_0/\cos\theta$, that corresponds to local spatial frequency $f_l = \lambda^{-1}\sin\theta$. Spherical waves of aliased points have the same local spatial frequency at coordinates corresponding to aliased sources. We therefore find aliased source position $\xi_A^{\pm}$ with

$$\begin{aligned} f_l(x') &= \frac{\partial\phi(x')}{2\pi\partial x'} = \frac{\partial R(x', \xi_A^{\pm})}{\lambda\partial x'} \\ &= \begin{cases} \lambda^{-1}\sin\theta + (\Delta)^{-1} & \text{for } x' = \xi_A^{+}/\cos\theta, \\ \lambda^{-1}\sin\theta - (\Delta)^{-1} & \text{for } x' = \xi_A^{-}/\cos\theta. \end{cases} \end{aligned}$$
$$(19)$$

Applying these criteria, we can compute positions of left and right alias sources in the reconstruction plane

$$\begin{aligned} \xi_A^{\pm} = \cos\theta(z\sin\theta + \xi_0^{\mp}\cos\theta \\ - \tan\gamma^{\pm}(z\cos\theta - \xi_0^{\mp}\sin\theta)), \qquad (20) \end{aligned}$$

where $\xi_0^{\pm}$ denotes the image point positions outside of the FoV ($\xi_0^{+} > \xi_{\text{FOV}}^{+}, \xi_0^{-} < \xi_{\text{FOV}}^{-}$) and $\gamma^{\pm} = \sin^{-1}(\sin\theta \mp (\Delta)^{-1})$.

In Fig. 9 we plot positions of point images in the region of possible FoV extension. We plot there the location of point sources and their corresponding aliasing sources, on the left and the right of the FoV. It can be noticed that the aliased image ξ_A^{+} is generated farther away from the FoV boundary than the ξ_A^{-}. Therefore, to find the limit of the FoV extension, we analyze the left region. We extend a holographic image from both left and right, and we examine if an aliasing image overlaps with an original one. The closest overlapping is at the right of the FoV extension. In Fig. 9 this corresponds to crossing of the line of the right source ξ_0^{+} and the alias ξ_A^{-}. We use this idea as a means of finding the limit of the FoV extension. We also keep in mind that the closest FoV extension corresponds to images with both higher image intensity and resolution. Application of the idea gives the condition for FoV extension:

$$\begin{aligned} \xi_A^{-} &= \cos\theta(z\sin\theta + \xi_0^{+}\cos\theta \\ &\quad - \tan\gamma^{+}(z\cos\theta - \xi_0^{+}\sin\theta)) \quad \text{for} \quad \xi_{\text{FOV}}^{+} \\ &< \xi_0^{+} < \xi_{\text{FOV}}^{+} + N\Delta\cos\theta. \end{aligned}$$
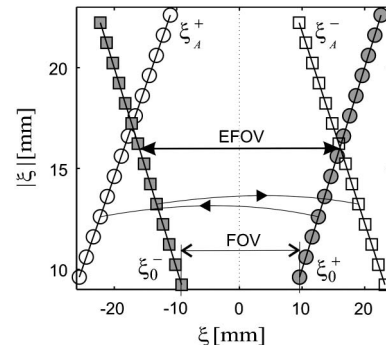$$(21)$$

Fig. 9. FoV extension for exemplary $\theta = 25°$ and $z = 500$ mm.

Fig. 10. (Color online) Image of a generated target (a) and its image reconstruction, (b) from CGH.

The condition gives bounds of the EFoV:

$$\xi_{\mathrm{EFOV}}^{\pm} = z \frac{\tan\theta - \tan\gamma^{\pm}}{1 + \cos^{-2}\theta + \tan\theta\tan\gamma^{\pm}}. \quad (22)$$

In Fig. 8, beside the limits of the FoV, limits of the EFoV are plotted with a dashed line for a tilt angle of 25°, where the magnitude of extension of the image area using the EFoV is seen.

It has to be mentioned that both aliased images are in slightly defocused planes. Alias ξ_A^+ characterizes negative defocus, while ξ_A^- a positive one. As a result, the alias images at the image plane are not in focus, and their intensity centers are shifted. However, the shifts are small ones, and the aliased images are outside of the EFoV. We have analyzed the magnitude of defocus with local spatial derivative as well. For confirmation, we have performed simulations and the experiment.

To verify theoretically predicted extension of an FoV, we have designed a CGH with the algorithm discussed in Section 4, for SLM inclination angle $\theta = 20°$ and image distance $z = 300\,\mathrm{mm}$. The hologram target and the result of its optoelectronic reconstruction are shown in Fig. 10. The reconstructed field was captured with a CCD detector placed at the image plane Ξ. The image was acquired with a long exposure time for the CCD camera, so the central reconstruction region was saturated and all aliased images are well visible. The region between two lines corresponds to the size of the EFoV. The image parts

outside of the EFoV generate aliased images that are in the EFoV disturbing imaging space.

7. Experiment

To illustrate the discussion given in Sections 3 and 4, we test both paper-developed algorithms: the digital hologram tilt correction algorithm and the CGH one for tilted display. The digital hologram tilt correction algorithm processes a hologram captured with normal orientation of CCD, so it can be displayed at a tilted SLM. For each tilt of the SLM, we apply proper aberration and the pixel correction matrices. To benchmark the algorithm, we have processed a hologram of a screw set. The digital hologram was captured for inline configuration with phase shift, so we have access to the complex object beam. We have first reconstructed the digital hologram directly in the display presented in Fig. 1 for SLM normal configuration ($\theta = 0°$). We address the SLM with phase of the digital hologram object wave. The real image was captured with a CCD. The result is presented in Fig. 11(a). We have processed the hologram with the tilt correction algorithm for various SLM tilts $\theta = 10°, 20°, 30°, 40°$. Then we reconstructed these holograms in the holographic display with corresponding SLM angular orientations. The reconstructed holograms were captured by a CCD camera, and they are presented in Figs. 11(b)–11(e). For comparison, in Figs. 11(f)–11(i) we present reconstruction of nonprocessed holograms for the same SLM tilts. It can be noticed that the loss in quality of reconstruction is small for processed holograms. Comparing both results, we can conclude that, even with large SLM tilts, we can obtain good-quality optical reconstructions of the digital hologram after application of the tilt correction algorithm.

To assess the quality of the developed CGH algorithm, we have generated and displayed holograms for a gargoyle statue given as a 3D numerical model. Therefore, we had access to any projection "photo." In Fig. 12 we present photos of optoelectronic reconstructions obtained for designed CGHs. To capture the images with a digital camera, we placed a diffusing screen at hologram reconstruction plane.
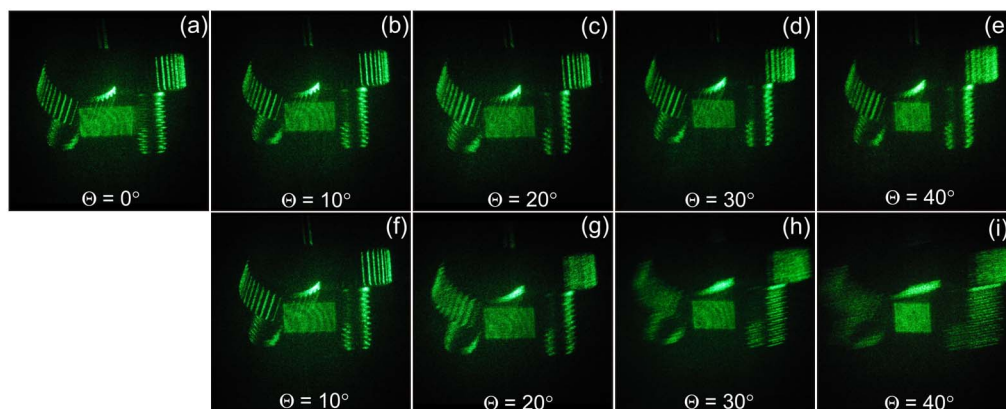

Fig. 11. (Color online) Comparison of image reconstruction obtained for digital hologram of screw set and series of SLM tilts: $\theta = 0°, 10°, 20°, 30°, 40°$; reconstructions (b)–(e) are obtained for processed holograms with tilt correction algorithm and (f)–(i) for unprocessed ones.
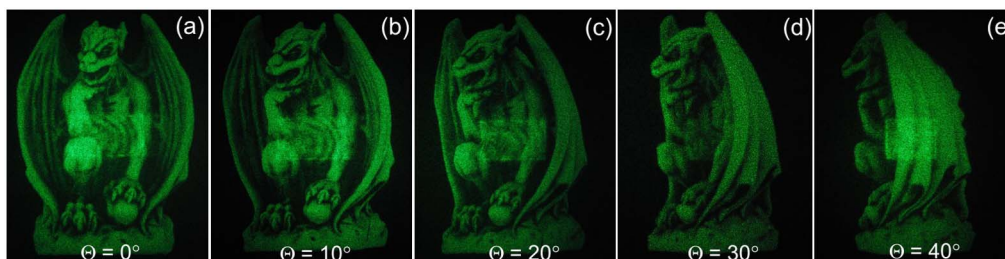
Fig. 12. (Color online) Comparison of image reconstructions obtained for CGHs of gargoyle statue designed for series of SLM tilts: $\theta = 0°$, 10°, 20°, 30°, 40° and corresponding statue perspectives.

CGHs were designed for different perspectives of the objects (0°, 20°, 30°, 40°) and the corresponding SLM tilts $\theta = 0°$, 20°, 30°, 40°.

8. Conclusions

This paper presents the holographic display utilizing a reflective phase-only LCoS-based SLM, where the SLM is illuminated with a highly inclined plane wave. We show that, even with highly off-axis illumination, the display can produce good-quality reconstructions. We have experimentally shown that digital holograms cannot be directly reconstructed in tilted geometry. For large tilts, such reconstructions are of very low quality. Therefore, utilizing rigorous propagation of paraxial fields between tilted planes, we have developed a digital hologram processing algorithm, where only the necessary paraxial holographic field is used. We have also shown that reconstructions of processed holograms are of high quality even for large SLM tilt. Observed loss of the imaging quality results from pixel cross talk exceeding 50% for a 30° tilt angle. In this paper we have developed an optimized CGH algorithm for tilted SLM geometry as well. We have presented its experimental performance. Additionally, we have performed an analysis of the FoV for a tilted SLM display. The analysis is based on local spatial frequencies and through study of the aliasing effect gives inclination-dependent FoV. To obtain good-quality reconstructions, we have optimized the imaging in the tilted SLM holographic display. The incidence angle affects SLM performance. In this paper, we have proposed a methodology for inclined SLM calibration of both factors: pixel response and wave aberration. Holographic display can generate images of real-world objects as well as the objects from the virtual world. Imaging of real-world objects captured by means of digital holography is more attractive.

References

1. D. Gabor, "A new microscopic principle," Nature **161**, 777–778 (1948).
2. H. M. Ozaktas and L. Onural, *Three-Dimensional Television* (Springer, 2008).
3. A. Michałkiewicz, M. Kujawińska, T. Kozacki, X. Wang, and P. J. Bos, "Holographic three-dimensional displays with liquid crystal on silicon spatial light modulator," Proc. SPIE **5531**, 85–94 (2004).
4. J. Hahn, H. Kim, Y. Lim, G. Park, and B. Lee, "Wide viewing angle dynamic holographic stereogram with a curved array of spatial light modulators," Opt. Express **16**, 12372–12386 (2008).
5. K. Maeno, N. Fukaya, O. Nishikawa, K. Sato, and T. Honda, "Electro-holographic display using 15 megapixels LCD," Proc. SPIE **2652**, 15–23 (1996).
6. G. Finke, T. Kozacki, and M. Kujawinska, "Wide viewing angle holographic display with multi spatial light modulator array," Proc. SPIE **7723**, 77230A (2010).
7. J. W. Goodman, *Introduction to Fourier Optics* 2nd ed. (McGraw-Hill, 1996).
8. A. Lizana, N. Martín, M. Estapé, E. Fernández, I. Moreno, A. Márquez, C. Iemmi, J. Campos, and M. J. Yzuel, "Influence of the incident angle in the performance of liquid crystal on silicon displays," Opt. Express **17**, 8491–8505 (2009).
9. T. Latychevskaia and H.-W. Fink, "Solution to the twin image problem in holography," Phys. Rev. Lett. **98**, 23390–23393 (2007).
10. I. Yamaguchi and T. Zhang, "Phase-shifting digital holography," Opt. Lett. **22**, 1268–1270 (1997).
11. J. J. Stamnes, *Waves in Focal Regions* (Hilger, 1986).
12. N. Delen and B. Hooker, "Free-space beam propagation between arbitrarily oriented planes based on full diffraction theory: a fast Fourier transform approach," J. Opt. Soc. Am. A **15**, 857–867 (1998).
13. K. Matsushima, H. Schimmel, and F. Wyrowski, "Fast calculation method for optical diffraction on tilted planes by use of the angular spectrum of plane waves," J. Opt. Soc. Am. A **20**, 1755–1762 (2003).
14. K. Matsushima, "Computer-generated holograms for three-dimensional surface objects with shade and texture," Appl. Opt. **44**, 4607–4614 (2005).
15. T. M. Lehmann, C. Gonner, K. Spitzer, "Survey: interpolation methods in medical image processing," IEEE Trans. Med. Imag. **18**, 1049–1075 (1999).
16. D. P. Kelly, D. S. Monaghan, N. Pandey, T. Kozacki, A. Michałkiewicz, B. M. Hennelly, and M. Kujawinska, "Digital holographic capture and optoelectronic reconstruction for 3D displays," Int. J. Digit. Multimedia Broadcast. **2010**, 759323 (2010).

17. J. R. Fienup, "Phase retrieval algorithms: a comparison," Appl. Opt. **21**, 2758–2769 (1982).
18. D. P. Kelly, B. M. Hennelly, W. T. Rhodes, and J. T. Sheridan, "Analytical and numerical analysis of linear optical systems," Opt. Eng. **45**, 088201 (2006).
19. R. Jóźwicki, "Transformation of reference spheres by an aberration free and infinitely large optical system in the Fresnel approximation," J. Mod. Opt. **29**, 1383–1393 (1982).
20. T. Kozacki, "Numerical errors of diffraction computing using plane wave spectrum decomposition," Opt. Commun. **281**, 4219–4223 (2008).
21. T. Kozacki, "On resolution and viewing of holographic image generated by 3D holographic display," Opt. Express **18**, 27118–27129 (2010).
22. V. Soifer, *Methods for Computer Design of Diffractive Optical Elements* (Wiley-Interscience 2001).
23. X. Xun and R. W. Cohn, "Phase calibration of spatially nonuniform spatial light modulators," Appl. Opt. **43**, 6400–6406 (2004).
24. A. Bergeron, J. Gauvin, F. Gagnon, D. Gingras, H. H. Arsenault, and M. Doucet, "Phase calibration and applications of a liquid-crystal spatial light modulator," Appl. Opt. **34**, 5133–5139 (1995).
25. A. Rohrbach and W. Singer, "Scattering of a scalar field at dielectric surfaces by Born series expansion," J. Opt. Soc. Am. A **15**, 2651–2659 (1998).
26. T. Kreis, *Handbook of Holographic Interferometry* (Weinheim, 2005).